Geophys. J. Int. (1999) **136,** 309–323

Vertical profile of effective turbidity reconstructed from broadening of incoherent body-wave pulses—II. Application to Kamchatka data

A. A. Gusev and I. R. Abubakirov

Institute of Volcanic Geology and Geochemistry and Kamchatka EMSD, 9 Piip Blvd, Petropavlovsk-Kamchatsky, 683006 *Russia. E-mail: ivgg@svyaz.kamchatka.su*

Accepted 1998 September 16. Received 1998 May 12; in original form 1997 July 2

SUMMARY

The vertical profile of effective turbidity under Kamchatka is reconstructed from observations of distance-dependent broadening of the inchoherent pulse of high-frequency body waves from small earthquakes, by means of a new approach and data processing scheme developed in Paper I. The key 'effective turbidity' parameter, g_e, used is an immediate generalization of the common isotropic turbidity/scattering coefficient g. Measurements of 200–600 onset-to-peak delays for P and S waves for five Kamchatka stations are used for interpretation. The estimates based on these data correspond to the 2–4 Hz frequency band. The inversion of data is performed in terms of the parameters of two generic vertical effective turbidity structures: a piecewise-constant profile (PCP) and truncated-inverse-power-law profile (TPLP), both used in several variants. The variants of the inversions give consistent results, but also reveal rather limited resolution, not permitting the recovery of detailed profiles or a comparison of results among individual stations. The inversions indicate that the values of effective turbidity decay from the surface down: within the depth interval $h = 0$–50 km, the decay is gradual; at greater depths it is much steeper, roughly following the inverse cube law. The estimates of average effective mean free path $l_e = 1/g_e$ are very close for P and S waves: 50–60 km (± 20 per cent) for the 0–20 km layer; 250–300 km (± 30 per cent) for the 20–80 km layer; and at $h > 60$–80 km, $l_e \approx 100(h/40)^{-2-4}$ for both P and S waves. The value of both the P- and the S-wave optical thickness (total scattering loss) of the upper 200 km is about 0.75 (± 25 per cent), and the lithospheric-scattering contribution to t_P^* is estimated as 0.2 s at 1 Hz. The expected S-wave scattering loss agrees reasonably with the standard regional amplitude attenuation curve, probably reflecting the secondary role of intrinsic loss at 3 Hz. The S-wave scattering Q in the lithosphere of Kamchatka is estimated for $f = 1$ Hz as 125, 205 and 255 for hypocentral distances of shallow events of 30, 100 and 300 km, respectively.

Key words: attenuation, inverse problem, inversion, scattering, seismic waves.

INTRODUCTION

There is a common understanding of the fast decay of the scattering capability of the Earth medium with depth, based on the analysis of teleseismic P waves (e.g. Aki 1973; Flatte & Wu 1988), but little is known about the details of the vertical distribution of scattering properties. Estimates of vertical turbidity structure were proposed by Rautian *et al.* (1981), who used regional S waves and codas. Gusev (1995) inverted data on apparent coda-wave attenuation and recovered the approximately inverse-power-law mode of decay of turbidity of scattering coefficient with depth ($\propto h^{-2-3}$), but did not estimate any absolute values.

A promising approach for the study of scattering, and especially of non-uniform scattering structure, is to use the broadening with distance of incoherent, noise-like high-frequency body-wave pulses. The rate of pulse-width increase with distance can be inverted in terms of scattering parameters (Gusev & Lemzikov 1983, 1985; Sato 1989). Abubakirov & Gusev (1990) found that, at a given hypocentral distance, pulse broadening is weaker for greater source depths, directly indicating the decay of scattering capability with depth.

© 1999 RAS

When analysing scattering properties of the Earth, it is convenient to employ a single parameter that might jointly describe various scattering-related phenomena: forward scattering, manifested in pulse broadening, back scattering, manifested in coda formation, and scattering energy loss. Fortunately, such a parameter, namely effective turbidity g_e, can indeed be introduced. It is in terms of this parameter that we will perform the actual inversions below. In a companion paper (Gusev & Abubakirov 1999; hereafter Paper I) this point is discussed in detail. Briefly, the g_e value describes scattering loss and coda formation, just as the isotropic turbidity value g does in the well-studied case of isotropic scattering; in addition, it describes pulse broadening, non-existent in that case. The effective mean free path, $l_e = 1/g_e$, essentially coincides with the 'isotropization distance' of Gusev & Lemzikov (1983, 1985); that is, the distance where forward-scattered energy, after a number of acts of forward scattering, is deflected by a cumulative angle of 1–2 rad from the initial direction of the unperturbed ray, and thus 'forgets' it, to propagate almost isotropically at later times.

The relationship between the effective turbidity of a medium and the broadening of a pulse that propagates through it was derived by Williamson (1972) for the case of a uniformly scattering medium, low-angle scattering and Gaussian autocorrelation of the inhomogeneity field. Bocharov (1988) generalized this result for the non-uniform case. In Paper I, we developed a method for data analysis based on the application of Bocharov's formula; it represents an inversion of layered turbidity structure based on linear least squares. We also analysed a few practical aspects of the application of the general approach to seismological data; in particularly, the correctness of the low-angle approximation, the use of peak-delay observations instead of the pulse centroid of Bocharov's formula, corrections for a realistic spatial spectrum of the inhomogeneity field, a potential bias produced by intrinsic loss, and the effects of a non-spherical, double-dipole source radiation pattern. The latter problem has the potential for significant data distortion; hence we proposed an efficient robust estimation procedure aimed at the suppression of such distortions. Finally, we tested the inversion procedure on synthetic data.

Below, we apply this general approach to the inversion of the pulse-broadening data for body waves from local Kamchatka earthquakes as expressed in the values of the onset-to-peak delay time. These data contain limited amount of information (they are rather noisy), and hence in our inversions we could use only simple models of the medium with vertically varying scattering properties. The parameters of such models will be estimated from the data sets of *P* and *S* waves of five seismic stations.

In a preliminary study, Gusev & Abubakirov (1996a) made the first successful attempt to perform the inversion of vertical turbidity structure from pulse delays on the basis of Bocharov's formula. Compared to the approach of that paper, in the present work we introduce significant modifications: we use realistic velocity structure, reject data from near-horizontal rays, and apply a robust estimation procedure based on residual-dependent data weighting. This yielded a significant improvement in the quality and reliability of the parameters of non-uniform turbidity structure obtained in the inversion.

The structure of the paper is as follows. We review the data processing procedure presented in detail in Paper I, and add an important generalization. We describe our data sets, and verify that the requirements needed for meaningful inversion are fulfilled. We then choose parametrizations for a turbidity profile. Two generic parametrizations are used in parallel: (1) a set of constant-g_e layers over a constant-g_e half-space, and (2) a constant-g_e layer overlying a half-space with inverse power law g_e decay. Next the results of the inversions for a number of data sets are analysed, first individually and then as a whole, and average estimates for vertical profiles of g_e under Kamchatka are compiled. Finally we compare our results with previous studies of scattering and attenuation in Kamchatka.

INVERSION ALGORITHM

We review the key equations of Paper I which present the basis for inversion. Denote by t_{mj} ($j = 1, 2, \ldots N$) the jth observed value of the body-wave onset-to-peak delay t_m assumed to be caused by forward scattering, and, by normalizing it by the corresponding traveltime t_{dj}, obtain modified data $y_j = t_{mj}/t_{dj}$ such that the variance of y_j can be assumed to be approximately independent of distance. Let the theoretical expression that relates y_{mj} to the vector of (unknown) parameters $\mathbf{p} = \{p_i\}$ of a particular parametric model be written as $Z_j(\mathbf{p})$. Then

$$Z_j(\mathbf{p}) + \varepsilon_j = y_{mj}, \tag{1}$$

where ε_j is the error, which combines data noise and model inadequacy. Consider first the case of a model that consists of a set of constant effective turbidity g_e layers over constant-g_e half-space. This model will be hereafter denoted as a piecewise-constant profile, or PCP. Let $i = 1, 2, \ldots M-1$ enumerate the layers counting from the surface down, and let $i = M$ correspond to the lower half-space. Let m be the number of the layer that contains the source. For $i = 1, \ldots, M$, $p_i = g_{ei}$. Let us introduce also the constant delay term $t_{m0} = p_0 = g_{e0}$ associated with $i = 0$.

To find the particular form of $Z_j(\mathbf{p})$ we directly evaluate Bocharov's integral formula (eq. 12 of Paper I) for the PCP case. Let us omit the j subscript. Let s be the coordinate along the unperturbed ray of total length S. The ray is calculated based on the known velocity structure. Let $g_e(s)$ be equal to constants $g_{e1}, g_{e2}, \ldots g_{eK}$ within corresponding ray segments $(0, s_1), (s_1, s_2), \ldots, (s_{m-1}, S)$ (assumed known from ray calculations). For this case, the cited formula yields

$$(c/S^2)\langle T\rangle = g_{e0} + g_{e1}U(0, \zeta_1) + g_{e2}U(\zeta_1, \zeta_2) + \ldots + g_{em}U(\zeta_{m-1}, 1), \tag{2}$$

where $\langle T\rangle$ is the mean pulse delay along the given ray, $\zeta_i = s_i/S$, and

$$U(p, q) = (p^2/2 - p^3/3) - (q^2/2 - q^3/3). \tag{3}$$

For the ray in question, s_i, S and ζ_i are known. To account for variable velocity, we simply set $c = S/t_d$ in (2).

Now assuming $\langle t_m\rangle/\langle T\rangle = 0.55 = B$ (see Paper I), for $Z_j(\mathbf{p}) = t_{mj}/t_{dj}$ write

$$Z_j = \sum_{i=0}^{M} a_{ij} g_{ei}, \tag{4}$$

where the coefficients a_{ij} are

$a_{0j} = 1/t_{dj}$;

$a_{ij} = BSU(\zeta_{i-1}, \zeta_i)$ for $i \le m$;

$a_{ij} = 0$ for $m+1 < i < M$.

For $N > M$, N equations (4) represent an overdetermined linear system, to be solved by least squares. Now denote the a_{ij} matrix as $\mathbf{A}$, the Z_j vector as $\mathbf{Z}$, and the matrix of residual-dependent weights (to be defined soon) as $\mathbf{W}$, and then for the least-squares estimate $\mathbf{p}'$ we obtain the standard result

$$\mathbf{p}' = (\mathbf{A}^T\mathbf{W}\mathbf{A})^{-1}\mathbf{A}^T\mathbf{W}\mathbf{Z}. \quad (5)$$

In the practical implementation this result is recalculated iteratively, with the diagonal $\mathbf{W}$ matrix adjusted based on residuals of the previous iteration, until convergence is reached. The starting state for $\mathbf{W}$ is the unity matrix, and the value of the weight for the next iteration is calculated by the formula

$$w_{jj} = w(\delta y_j) = 1/[(1 + q(|\delta y_j|/\sigma)^\beta], \quad (6)$$

where δy_j is the residual of y_j, and σ^2 is the weighted estimate of the variance of ε_j, both obtained on the current iteration; q and β are adjustable constants, set to $q = 2.3$, $\beta = 4$.

A further turbidity profile parametrization was also used, consisting of a layer with constant g_e over a half-space with the inverse power-law g_e decay:

$$g_e(h) = \begin{cases} G, & 0 < h < H, \\ G(H/h)^\chi, & h > H; \end{cases} \quad (7)$$

it is denoted as the 'truncated inverse power law' profile (TPLP). The analogue of eq. (4) for this case is

$$Z_j = a_{0j}g_{e0} + a_{1j}g_{e1}, \quad (8)$$

where $a_{0j} = 1/t_{dj}$, $g_{e0} = t_{m0}$, $g_{e1} = G$. The coefficient a_{1j} is again obtained by direct integration. Its expression is somewhat lengthy, even for the simple 'single layer over half-space' velocity structure assumed here, and it is given in Appendix A.

DATA DESCRIPTION

The first stage of data analysis is to accumulate input observational data. For each station/body-wave type combination analysed, we use the values of onset-to-peak delay time, t_m for a large number of small earthquakes. To measure t_m values, we used records of local events of the five stations of the regional Kamchatka network: SPN, PET, TOP, BER and KRI (Fig. 1). The instruments are three-component 1.2 s pendulums of SM-3 type, combined with GB-IV type galvanometers of 0.07 s period; they employ photographic recording of 2 mm s^{-1} speed. The system response is practically flat for displacement between 1 and 10 Hz. Body-wave groups of regional events are relatively wide-band, and the typical visual frequency varies somewhat among records. However, this frequency is practically always inside the 1.5–6 Hz range, and typically is 2–5 Hz. For KRI, the typical frequency is somewhat higher (5–9 Hz). In a previous study (Abubakirov & Gusev 1990), it was found that, within the discussed frequency range, effective turbidity estimates determined separately for the 1.5, 3, and 6 Hz bands of the multi-band 'ChISS' instruments of SPN and PET vary only slightly. This permits us to use unfiltered displacement data with confidence, and to ascribe our results

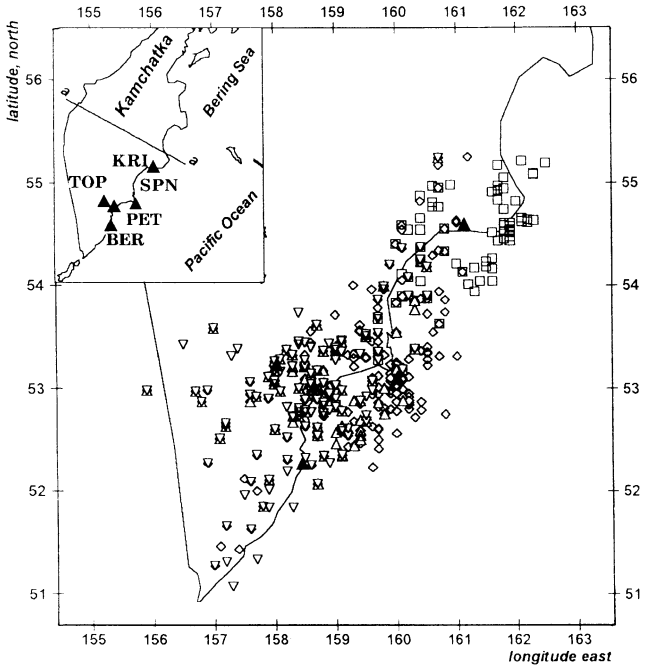

Figure 1. The region studied. Triangles: stations used in the data analysis (seen clearly on the insert). The symbols denote epicentres of events recorded at different stations; these records were used in the study.

quite safely to the 2–5 Hz frequency band, or equivalently, to the vicinity of the 3 Hz typical frequency.

Let us now estimate the expected range of the constant term t_{m0} for our data. Generally, it includes instrument-, source- and station-related delays. We estimate the first two contributions here. The station terms is difficult to find *a priori*; however, it may be assumed zero for a 'good' seismic station (see discussion in Paper I). Given the value of the upper cut-off frequency of the instrument transfer function of about 15 Hz, the corresponding mean pulse delay is of the order of 0.04 s. The source-related pulse delay is about half the visual signal period (typically 0.2–0.5 s) and can be estimated as 0.1–0.25 s. The total effect of the instrument filter and a source is about 0.15–0.30 s. The peak delay must be somewhat smaller than the mean delay, and is assumed to be equal to 0.8 of the mean delay, or 0.12–0.24 s. To constrain this parameter, we will use the value of 0.18 s. Such a constraint will systematically be applied later, because the information content of our data does not permit independent estimation of constant station terms.

The measurements of t_m were performed using hundreds of records from 1985–1995, on all three components, for *P* and *S* wave groups. It is easy to identify peaks for both *P* and *S*, and the onset for *P*, but the case of the *S*-wave onset is more complicated. It is not unusual for this onset to be emergent, and for its reading not to be fully reliable. To understand the importance of this problem, for 150 records we determined t_m in two ways: based on the visual *S* onset, and based on its expected arrival time, calculated using the traveltime table from the known hypocentre and origin time. We found no systematic errors. We performed effective turbidity inversion of PCP type (see below) for both data sets; the layer effective turbidity estimates calculated from each set differed by

5–10 per cent. On the basis of this test, we confine ourselves to t_m values based on the visually identified onset only.

To exclude problems related to multiple-ray propagation, the incidence angle at the source was limited to $<70°$. Fig. 1 shows all the epicentres of the earthquakes used in the analysis; Fig. 2 shows hypocentres on a cross-section across the island arc; in both cases we show the *P*-wave data coverage. Fig. 3 shows the distribution of individual data for *S* waves over depth and epicentral distance and also on t_m–hypocentral distance plane. *P*- and *S*-wave data coverage is similar. For SPN, PET and TOP, data sets are larger and include a proportion of rare events at depths 160–300 km, found by extending the data search over additional years of the catalogue. Among these 'better' stations, data coverage over distance is most even for SPN, and worst for TOP, where data are almost lacking at small hypocentral distances. (This problem is present for all the stations in varying degrees; it is inherent for island-arc type data where almost all events are located within the rather narrow inclined Benioff zone—see Fig. 2.) For BER and KRI, data sets do not include events at depths below 160 km; therefore, these stations are of secondary value.

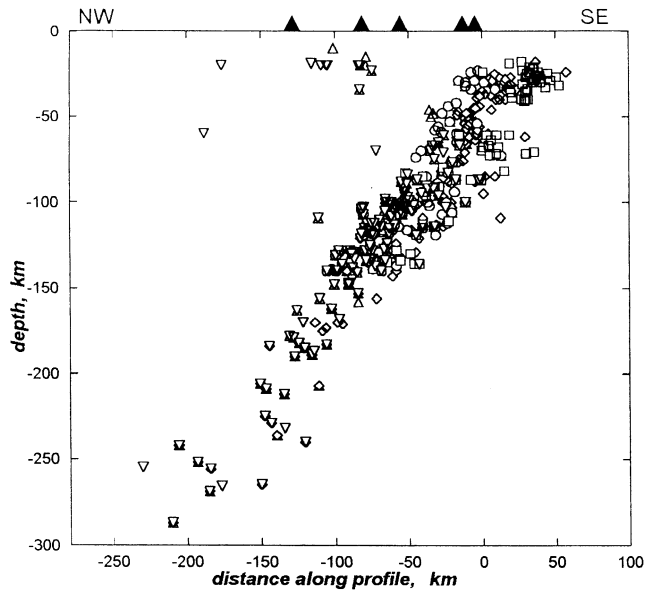

Figure 2. Cross-section view of event hypocentres (symbols) and stations (triangles) used, projected onto the vertical plane denoted *aa* on the insert map of Fig. 1.

To calculate rays, we first used the standard Kamchatka velocity profile: $c_P = 4$, 5.8, 6.7, 7.8 and 8.1 km s^{-1} for depth intervals 0–5, 5–20, 20–35, 35–120 and 120+ km; $c_S = c_P/1.73$ with the PCP model. However, we could not use such a detailed profile with the TPLP model. For the sake of uniformity we used in both cases a simplified velocity profile with $c_P = 6$ km s^{-1} over the 35 km crust and $c_P = 7.8$ km s^{-1} over the mantle. The differences between the results of inversion based on the 'accurate' and 'simplified' velocity profiles were estimated by comparison of two PCP inversions with similar data sets; these differences were no more than 3 per cent and considered negligible; thus for all further inversions we used the 'simplified' velocity profile.

ANALYSIS OF APPLICABILITY OF THE METHOD

Before performing the inversions proper, we must first verify the applicability of Bocharov's theory. The theory has been developed for the case of the low-angle approximation, zero intrinsic loss, and a spherically symmetric source radiation pattern, whereas all these conditions are more or less violated, and an analysis is necessary. Other possible problems (see Paper I for the complete list) are not so critical as to deserve detailed discussion, and will be referred to as necessary.

Low-angle approximation

For our data, the delay of a pulse peak is 1–10 s, to be compared to propagation times of 10–40 s and greater. In other words, y_j is typically below 0.1, and its rms value is about 0.03. Thus the low-angle approximation is valid.

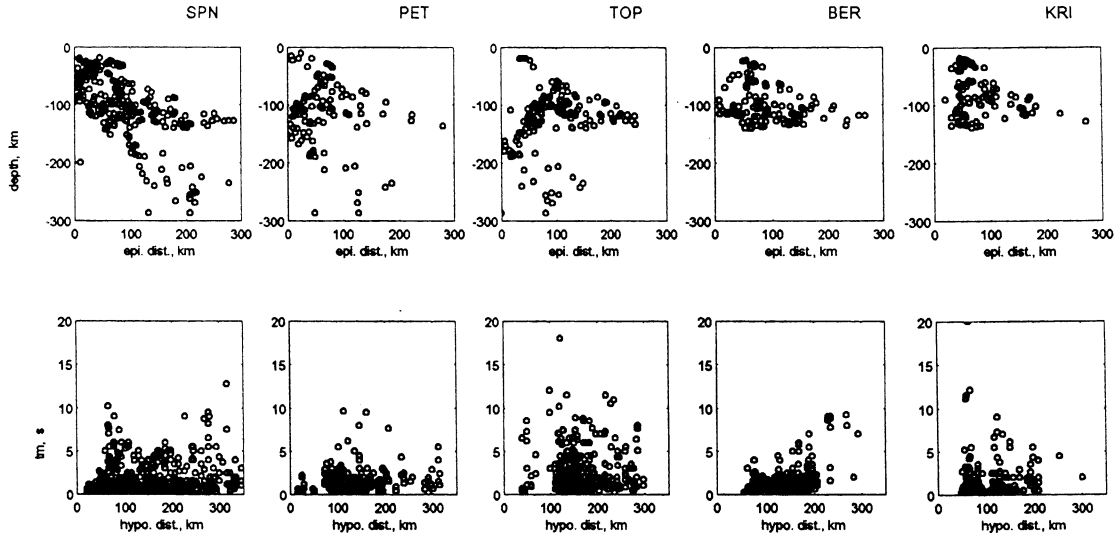

Figure 3. Data coverage for *S*-wave data for five stations used, on depth versus epicentral distance plane (upper row) and on t_m versus hypocentral distance plane (lower row).

Intrinsic loss effect

To understand the importance of the possible biasing effect of intrinsic loss on pulse broadening, we calculated it for Williamson's (1972) theoretical pulse shape. For $f = 3$ Hz, we assumed the realistic values of $l_e = 50$–100 km, and of intrinsic Q as $Q_i = 350$, [equal to coda Q (3 Hz) for Kamchatka, after Abubakirov & Gusev (1990)]. For this case, the expected t_m value decreases by at most 25 per cent at the considerably large distance of 250 km, and the slope of the t_m versus distance log–log relationship over the 50–250 km distance interval changes from 2 to about 1.8. At a distance of 100 km, the error in t_m is -8 per cent. However, these estimates are unrealistically large. For a self-similar inhomogeneity field with the properties found by Gusev & Abubakirov (1996b), the actual pulse must have an onset-to-peak delay of about half the value calculated for the Gaussian ACF case (the one for which the Williamson's shape function is relevant) for the same optical distance. As the distortion introduced by intrinsic loss increases in time, decreasing the delay by half will reduce this distortion by at least half as well. In addition, the Q_i value of 350 was estimated in the framework of the model of uniformly scattering medium and thus is much too low. The more realistic estimate of $Q_i = 1000$–2000 (Dainty 1981; Gusev 1995) may be more adequate. The use of $Q_i = 1000$ would reduce the error of the kind discussed to a completely negligible level.

Regular and outlier components of data

As explained in Paper I, to perform a meaningful inversion one must suppress the biasing effect of near-nodal arrivals: they have small initial amplitudes and large onset-to-peak delays whose origin is irrelevant to scattering. Planning this suppression needs preliminary data analysis. Also, the data normalization by traveltime mentioned in relation to eq. (1) needs experimental support. To understand these problems, the statistical structure of the data should be studied. However, to do this reliably we need the results of a reasonable inversion, and to perform such an inversion we must have a prior understanding of the data statistics. This situation is not completely circular, however, because the weighting scheme exemplified by (6) is not merely a workable trick: it is a statistically well-founded procedure (Jeffreys 1961) and it works automatically if the rather general initial assumption is valid, that data is a mixture of low-variance and high-variance subpopulations. For this reason, we can safely use the residuals resulting in some reliable inversion to illustrate the validity of our assumptions regarding data structure.

To implement this idea, we carried out inversions for the TPLP structure with fixed values of $H = 40$ km and $\alpha = 3$, which are close to our final estimates obtained below. We analyse the residuals combined from two inversions for stations SPN and PET. The general data scatter can be seen in Fig. 4, where t_m versus traveltime and y versus traveltime data are depicted. First of all a large data scatter is apparent, with absolute deviations of up to 10 s and more. After a more detailed examination, it can be seen that there is a mixture of two distributions: (1) a small-dispersion component, concentrated around zero, moderately asymmetrical and interpreted as 'regular errors', and (2) a highly asymmetrical large-dispersion component, interpreted as 'outliers' produced by near-nodal data. The robust inversion procedure that produced the plotted residuals has essentially classified the data into these two groups. The two horizontal lines on each plot are approximate 1 per cent quantiles ($q = 2.3$) of the 'regular' component approximated by the normal law. In both cases,

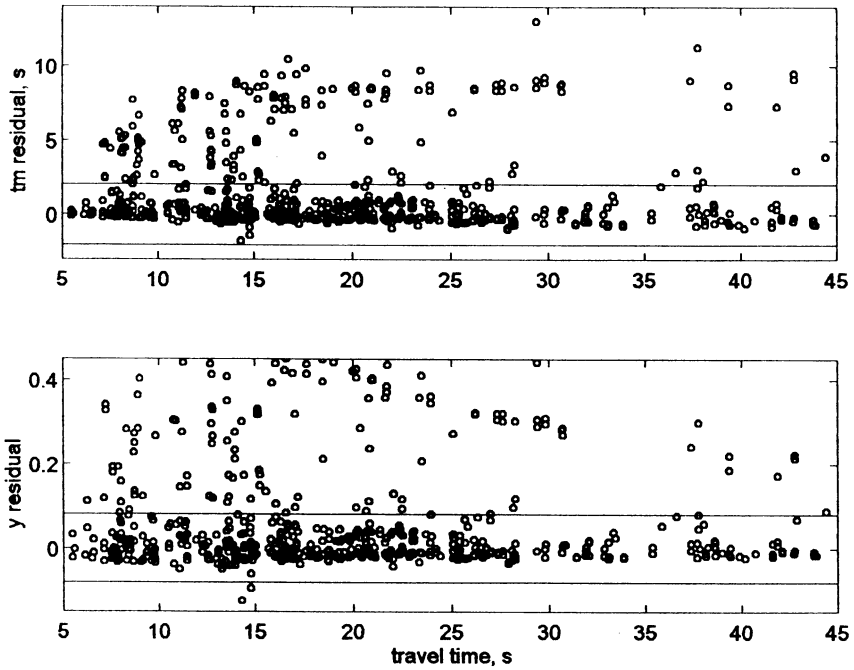

Figure 4. Inversion residuals combined for *P*-SPN and *P*-PET data sets, plotted versus traveltime. Lower plot: residuals of 'normalized' y values actually used for inversion; upper plot: residuals of 'raw' t_m values calculated within the same inversion. Data may be thought as a mix of 'regular' and 'outlier' components. Horizontal lines denote approximate bounds for the 'regular' component.

the value of the variance σ^2 of the regular component was estimated from the data. The lines mark the points where the weighting function (6) used becomes lower than 0.5. Fig. 5 shows the observed distributions of δy as a histogram. It can be seen that the *P*-wave data are much more contaminated than the *S*-wave data; this agrees with the fact that the *P*-wave radiation pattern of a double dipole has wider and deeper lows than that for *S* waves.

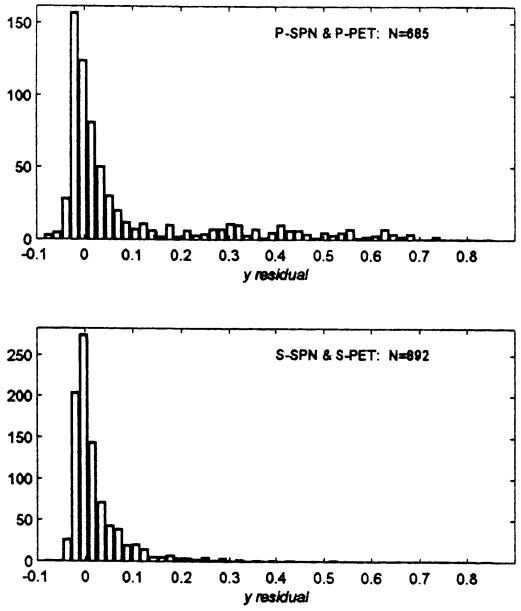

Figure 5. The distributions of y residuals (upper plot: those of Fig. 4). The mixed nature of these distributions, consisting of a 'regular' component (the asymmetric peak) and an 'outlier' component (the low plateau at positive values, much stronger for *P* waves), is evident.

Considering only the 'regular' component of Fig. 4, one may suspect that its scatter increases with distance for t_m and is more stable for y, but this is far from evident. Fig. 6 shows histograms for these residuals, drawn separately for small and large traveltimes. For t_m, the scatter of residuals evidently increases with distance, whereas the y residuals are relatively stable. This supports our choice of y and not t_m as the input data for inversion.

In Paper I we explained the large proportion of 'outlier' data by the effect of the double-dipole radiation pattern. Compared to the theoretically analysed case of a spherical radiation pattern, a station/component has in this case a significant probability of being near to the nodal direction and thus of having a negligible direct-wave amplitude. The peak in such a case is formed by sideways leaking of wave energy initially radiated in other directions (along curved rays), and its delay, although intrinsically caused by scattering, has no relation to the scattering-related broadening discussed here. Whereas low-amplitude, delayed-peak arrivals are quite commonly observed near nodal planes at least for *P* waves, it happens, unfortunately, to be very difficult to illustrate this fact by examples from our data set. The reason is that the Kamchatka network is rarefied (typically, 100–150 km between instruments), so accurate nodal plane solutions exist only when many reliable teleseismic signs are present. This means, practically, that $M > 5.5$–6. Such events usually have considerable source-related durations and thus have been excluded from our analysis.

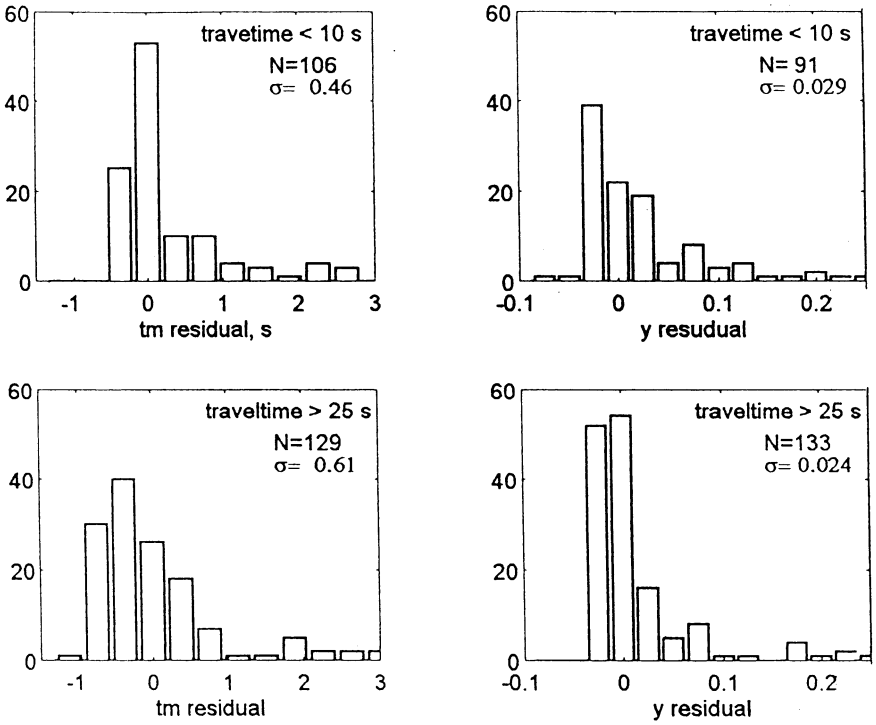

Figure 6. Histograms of residuals of t_{mj} (left column) and of y_j (right column) from Fig. 4 for small (upper plots) and large (lower plots) distances. The values of standard deviation are calculated only within the horizontal lines of Fig. 4 and, approximately, characterize the 'regular' component only. One can see the relatively stable scatter of y_j as opposed to the increase of scatter of t_{mj} with distance.

DATA ANALYSIS

The choice of parametrization for model profiles and the outline of the data analysis procedure

We are now ready to perform data processing proper. This needs, however, some preliminary planning. The final aim of the station data processing is to estimate the vertical profile of effective turbidity $g_e(h)$ under the seismic station. This is attained through the following stages: (1) specify the structure of a g_e model profile to search for, and introduce the vector $\mathbf{p}$ of unknown parameters for this model; (2) for each event, calculate the seismic ray in a known velocity structure, and check whether each datum corresponds to an uprising ray, and not to a nearly horizontal or reflected ray; (3) perform the inversion proper. Generally speaking, we would prefer to obtain as detailed a $g_e(h)$ as possible. In practice, however, we must represent $g_e(h)$ by a finite number of parameters. Unfortunately, as we will soon see, the real resolution permitted by the data is rather limited, and can be expressed by only a small number of independent unknown parameters (degrees of freedom), between 4 and 2.

There are data inversion approaches, exemplified by the singular value decomposition (SVD) technique, that permit decoupling of the number of parameters and the number of degrees of freedom, at the price of using correlated parameters. Thus by using SVD we might, to a large degree, get rid of the problem of the choice of parametrization of the model; instead, however, we would add to the already complicated problem under study all the technical intricacies of SVD. In the present novel attempt to invert g_e structure we preferred to use the more transparent technique of common least squares (LS). The actual LS procedure used includes iterative residual-dependent weighting (6) to make it robust.

Two different parametrizations, or generic model profiles, have been used. The first is a piecewise-constant profile (PCP), which consists of a number of constant-g_e layers over constant-g_e half-space. This structure is chosen as simple and easily invertable by linear least squares. When layer boundaries are fixed, the number of parameters in this model is $M+1$, where M is the number of layers. The weak point of this model is the unrealistic constant-g_e lowermost half-space. On the basis of results of Rautian *et al.* (1981) and Gusev (1995) one would rather expect a fast decay of turbidity over the whole depth range studied, with the possible exception of a surface layer. In view of this expected behaviour, it was suitable to incorporate the vertical decay of turbidity into the model. The important advantage of such a model is that it permits consistent estimation of integral scattering loss over the whole crust and upper mantle, whereas any model with a constant-g_e lower half-space is completely inadequate for this purpose. The particular model used that incorporates the expected vertical decay of turbidity is the TPLP one (7). This particular kind of structure has recently been proposed by Gusev (1995) based on the interpretation of coda-Q data, and one of the aims of the application of this model was merely the determination of its parameters from a new kind of data. With TPLP, there are three unknowns, G, α and H, and the problem is non-linear with respect to the two last variables. Hence, to find a solution, we will apply a common grid search over α and H, and combine it with least squares with respect to G.

When applying LS to data analysis one has to determine, for each data set, the number of degrees of freedom/independent parameters it can meaningfully provide. In regular cases, one can use such strategies as, for example, Fisher F statistics with respect to residual error variance, to determine the actual number of degrees of freedom. Unfortunately, this standard approach cannot be immediately generalized for the case of the residual-dependent weighting. For this reason, we used a more primitive approach, checking the sign and relative error (measured by coefficient of variation CV; that is the rms error of a value divided by itself) of layer g_e estimates, and considering the result unreliable when negative g_e estimates and/or large CV appear.

In our approach, the choice of layer boundaries is important. There are several lines of reasoning that determined our final set of boundaries. First, because of the general decay of turbidity with depth, it is unreasonable to divide the whole 300 km layer covered by data into parts of comparable size, say 150 and 150 km for two layers, because the contribution of the deeper layer is expected to be relatively very small and thus hardly resolvable. It seems better to divide the whole depth range into layers with, roughly, comparable contributions to the total delay. Assuming, for example, the inverse square law for the depth decay of turbidity, we arrive at the requirement that the layer thickness must increase with depth as the depth squared. This approach will at the same time produce a set of boundaries that are reasonable from the second point of view; that is, meeting the requirement that more or less comparable amounts of data be present in each layer (because of the properties of real seismicity, data density quickly decays with depth below $h=80$ km despite the special efforts described above). These two general requirements could not, however, be met simultaneously for the uppermost part of the profile, because of the lack of data for small depths, and, in the most detailed inversion, the 0–10 km layer lacks data points.

Another way to choose layer boundaries is to use our previous experience. For the case of a single-layer over half-space model, Gusev & Abubakirov (1996a) performed three-parameter inversion of Kamchatka data with a variable, unknown, value of layer thickness, and found that the optimal single-layer depth is between 20 and 45 km. One more consideration is to take into account the typical crustal depth in Kamchatka, of 30–35 km, and to use the Moho depth as a candidate boundary depth. Based on all this reasoning, we chose 35 km as the value of the layer thickness for the single-layer model. For the two-layer model, this single boundary was split into two at 20 and 80 km. For the three-layer model, we retained the 35 km boundary, and added 10 km and 100 km boundaries. The particular positions of the 10, 20, 80 and 100 km boundaries have no geological meaning, and are chosen based on our general approach. As for the TPLP model, the layer thickness was either estimated from data, or, for less-informative data sets, was fixed at 40 km for the reasons explained below.

One might expect to improve somewhat the reliability of inversion if it were possible to colocate layer boundaries with those known from other structural data, for example seismic structure. In this connection, it should be noted that the relationships between effective turbidity and other better-studied structural properties of the Earth medium are essentially unknown. In addition, the structure of a subduction zone, for example Kamchatka, is complicated and its most prominent

element—the interplate interface—is not horizontal. For these reasons, with the exception of the Moho, we were not able meaningfully to incorporate geological information into the choice of layer boundaries.

As was noted above, in both the PCP and TPLP cases, there is one more unknown, namely the distance-independent, constant pulse delay t_{m0}. With a very limited number of degrees of freedom in the data, it would be very useful to get rid of this unknown, fixing its value in some reasonable way. This will be done with the use of the *a priori* estimate obtained above.

Finally, we list all the variants of inversion that will be presented. Consecutive numbers will be used systematically to enumerate models, inversions and tables with their results. We begin with the PCP model and successively analyse the cases of one, two and three layers. The single-layer case is the test one: if a meaningful inversion for a data set cannot be performed with only two unknowns, the data set is hardly usable at all. In this case only we analyse the following possibilities: (1) not to apply the residual-dependent weighting; and (2) not to constrain the value of t_{m0}. Next the two- and three-layer cases are analysed, and for each data set we note at what number of unknowns the instability of inversion arises. The inversions, then, are as follows.

(1) PCP model with a layer (35 km crust) over a half-space (mantle).

(2) PCP with two layers and a half-space; boundaries set at 20 and 80 km.

(3) PCP with three layers and a half-space; boundaries set at 10, 35 and 100 km.

The four-parameter Inversion 3 is on the brink of instability even for the best data sets. Next, we pass to the TPLP model and perform inversion with three, two or even one (G) unknown:

(4) TPLP with three unknowns: H, α and G. This inversion is relatively stable for the best data sets only.

(5) TPLP with constrained $H = 40$ km; two unknowns: α and G.

(6) TPLP with constrained $\alpha = 2.5$; two unknowns: H and G, and also one unknown (G) in the two noisiest data sets.

In both Inversions 5 and 6, the aim is to obtain stabilized estimates where those of Inversion 4 are doubtful.

When analysing the results of inversions one should keep in mind the geophysical constraints on the unknowns: t_{m0} and all g_{ei} must be positive, and solutions with non-monotonic depth decay of g_e are less probable (but not impossible). A graphical illustration of the inversion procedure is given for Inversion 4 in Fig. 7; generally, the plots for different inversions differ only slightly.

Inversions of individual data sets

Inversion 1 (Table 1)

The results of this and other inversions are given in tables of similar structure. Table 1 contains: data volume N (similar for all inversions), rms residual ψ of y_j in per cent, average weight w_{av}, two estimates of effective turbidity: g_{e1} (layer) and g_{e2} (half-space), and estimated t_{m0}. The value of w_{av} may be viewed as the proportion of data not rejected, because the residual-dependent weighting function (6) changes from values of about unity to values of about zero rather abruptly. Because of the very large range of g_e values, we prefer to describe the accuracy through relative errors, rather than through absolute ones. Thus, all estimated parameters are accompanied by formal relative errors, expressed as coefficients of variation (defined as usual as standard deviation/estimate). We cite them for general orientation; as one can see from simulated examples in Paper I, they should not be given a large amount of credit as they may significantly underestimate real inaccuracies. In tables 2–6 we also give estimated values of effective optical thickness L_e of the profile; all these estimates will be discussed

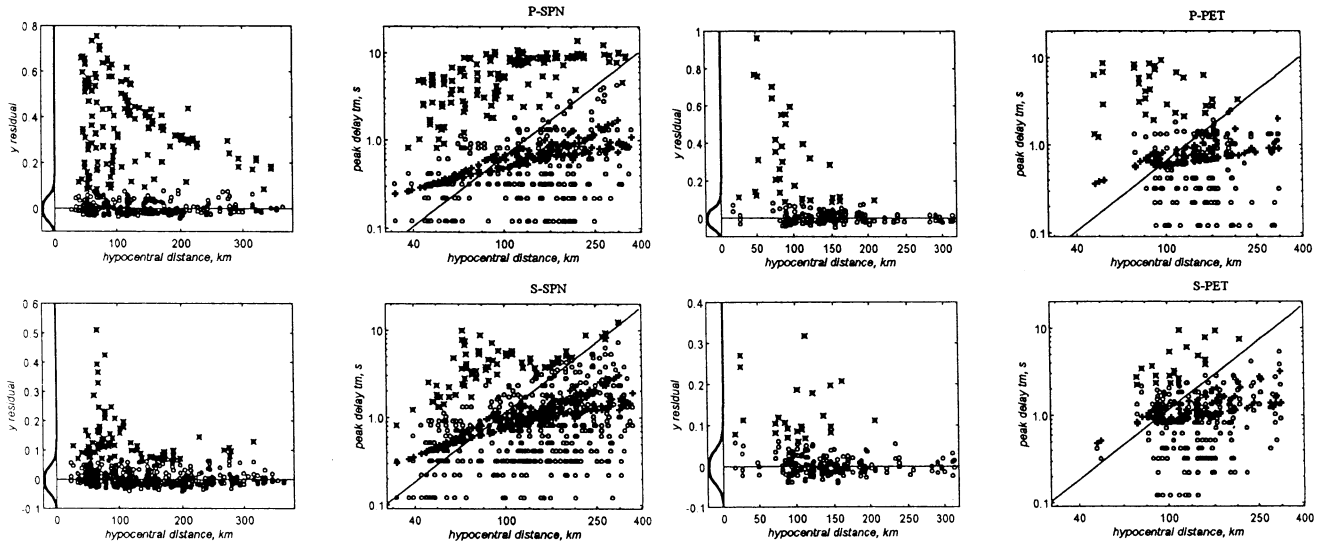

Figure 7. Illustrations for inversion 4, for stations SPN and PET, for P and S waves. ○ and × signs denote data points 'accepted' (i.e. with weight above 0.3) or 'rejected' (weights below 0.3). Columns 1 and 3: residuals of y versus hypocentral distance; the graph of the actual weighting function is plotted along the vertical axis on the left. Columns 2 and 4 t_m versus hypocentral distance. + denotes a theoretical t_m value. The reference line shows a quadratic trend characteristic for constant-g_e medium.

Table 1. Inversion 1: PCP model, one layer (0–35 km) over half-space*.

Data set	N	100ψ	w_{av}	g_{e1} & CV		g_{e2} & CV		t_{m0}(s) & CV	
P-SPN	478	18.73	1	45.7	0.12	0.91	0.87	−0.03	7.43
		2.67	0.64	10.7	0.09	0.23	0.50	0.05	0.78
S-SPN	630	5.70	1	18.4	0.08	0.01	15.2	−0.04	2.43
		2.16	0.80	4.14	0.17	0.59	0.13	0.37	0.12
P-PET	207	13.91	1	37.1	0.12	−2.68	0.34	0.31	0.60
		2.70	0.79	7.90	0.14	0.45	0.40	0.27	0.13
S-PET	262	4.71	1	5.64	0.27	0.56	0.56	0.73	0.13
		2.00	0.84	5.75	0.12	0.46	0.28	0.44	0.10
P-TOP	316	12.29	1	−12.51	0.80	1.74	0.38	3.06	0.14
		9.48	0.89	−17.83	0.43	1.57	0.32	2.92	0.11
S-TOP	375	8.97	1	10.87	0.60	0.69	0.71	1.39	0.36
		3.23	0.81	10.43	0.22	0.95	0.18	0.24	0.76
P-BER	198	13.42	1	20.18	0.39	−2.53	0.48	0.94	0.50
		3.63	0.79	2.36	1.00	−0.22	1.57	0.70	0.21
S-BER	362	3.50	1	10.29	0.20	1.74	0.15	−0.22	1.01
		1.95	0.85	6.33	0.19	1.04	0.14	0.03	4.11
P-KRI	164	18.42	1	4.58	0.22	−4.53	0.53	−0.38	1.55
		4.66	0.72	8.32	0.43	0.13	4.13	0.21	0.91
S-KRI	229	10.70	1	14.11	0.46	−0.31	3.04	0.22	2.84
		1.75	0.76	3.63	0.30	0.90	0.17	0.17	0.60

* For each data set, two inversions are presented as two lines. Upper line: no weighting is applied; lower line: standard weighting. g_{ei} values in $10^{-3}\,km^{-1}$ units.

Table 2. Inversion 2: PCP model, two layers (0–20 and 20–80 km) over half-space.

Data set	100ψ	w_{av}	g_{e1}, $10^{-3}\,km^{-1}$	g_{e2}, $10^{-3}\,km^{-1}$	g_{e3}, $10^{-3}\,km^{-1}$	CV(g_{e1-3})			L_{200} & CV(L_{200})	
P-SPN	2.61	0.63	9.76	1.41	0.162	0.084	0.146	1.21	0.37	0.084
S-SPN	2.29	0.81	9.53	1.86	0.042	0.073	0.084	3.33	0.38	0.061
P-PET	2.86	0.80	(22.89)	(1.12)	0.277	0.101	0.378	1.03	(0.68)	0.072
S-PET	2.06	0.84	9.70	2.26	0.086	0.111	0.103	2.54	0.43	0.085
S-TOP	3.38	0.81	10.71	2.68	0.905	0.165	0.102	0.28	0.62	0.077
S-BER[$]	1.92	0.85	(5.07)	(2.20)	(−0.70)	0.154	0.101	0.80	(0.18)	0.477
P-KRI[$]	4.65	0.72	(11.02)	(1.85)	(−0.90)	0.119	0.374	2.42	(0.26)	1.321
S-KRI	1.71	0.76	4.13	1.53	0.042	0.113	0.128	14.2	(0.23)	0.412
P-ave.			9.7	1.4	0.21				0.37	
S-ave.			8.5	2.1	0.27				0.47	

[$] Considerable negative g_{e3}, unreliable result.

Table 3. Inversion 3: PCP model, three layers (0–10, 10–35 and 35–100 km) over half-space.

Data set	100ψ	w_{av}	g_{e1}, $10^{-3}\,km^{-1}$	g_{e2}, $10^{-3}\,km^{-1}$	g_{e3}, $10^{-3}\,km^{-1}$	g_{e4}, $10^{-3}\,km^{-1}$	CV(g_{e1-4})				L_{200} & CV(L_{200})	
P-SPN[$]	2.60	0.63	9.6	6.04	0.66	0.13	0.51	0.21	0.37	1.82	0.37	0.12
S-SPN[$]	2.25	0.81	10.2	5.31	1.22	(−0.14)	0.33	0.16	0.14	1.22	0.37	0.08
P-PET[$]	2.67	0.80	10.1	6.97	1.59	(−0.17)	0.51	0.24	0.29	1.97	0.45	0.13
S-PET[$]	2.02	0.84	5.0	8.53	0.84	(0.17)	0.70	0.13	0.34	1.60	0.41	0.10
S-TOP[#]	3.14	0.81	(−3.6)	(17.2)	(−0.2)	(1.25)	1.29	0.11	2.13	0.23	(0.64)	0.07
S-BER[#]	1.93	0.85	(−7.1)	(8.4)	90.480	(1.30)	0.60	0.15	0.59	1.02	(0.39)	0.44
P-KRI[#]	4.70	0.73	10.9	8.20	(0.54)	(−2.61)	0.64	0.34	1.79	2.15	(0.05)	13.5
S-KRI[#]	1.71	0.76	6.7	2.08	(1.46)	(−2.62)	0.32	0.42	0.17	0.58	(−0.11)	2.2
P-ave.			10.2	7.0	1.1	—					0.41	
S-ave.			7.3	5.4	1.0	—					0.39	

[$] g_{e4} error above 100 per cent, g_{e4} considered unreliable, other g_{ei} considered acceptable.
[#] Large errors, negative g_{ei} estimates, inversion unreliable.

Table 4. Inversion 4: TPLP model, search over both H and α parameters.

Data set	100ψ	w_{av}	α	H km	G & CV 10^{-3} km^{-1}		L_{200}	L_{1000}
P-SPN	2.52	0.63	4	40	4.43	0.048	0.30	0.30
S-SPN	2.21	0.81	2	30	5.07	0.033	0.35	0.38
P-PET	2.60	0.78	3	70	3.00	0.062	0.37	0.38
S-PET	1.98	0.84	4	40	7.25	0.040	0.40	0.40
S-TOP[#]	3.28	0.81	1.5	20	9.61	0.042	0.58	0.67
S-BER[#]	1.89	0.84	5	50	3.27	0.043	0.26	0.26
P-KRI[#]	2.88	0.62	5	90	2.19	0.103	0.33	0.33
S-KRI[#]	1.71	0.76	1	20	3.41	0.057	0.49	0.45
aver.			3.3	45				
P-ave.			3.5	55			0.32	0.34
S-ave.			3	35			0.37	0.39

[#] Among these four data sets, there is close positive correlation between H and α indicating unstable inversion; only SPN and PET results included in the average.

Table 5. Inversion 5: TPLP model, $H = 40$ km constrained; search over α parameter.

Data set	100ψ	w_{av}	α	G & CV 10^{-3} km^{-1}		L_{200}	L_{1000}
P-SPN	2.52	0.63	4	4.42	0.048	0.30	0.30
S-SPN	2.53	0.80	4	4.72	0.034	0.32	0.32
P-PET	2.61	0.79	2	4.84	0.062	0.40	0.42
S-PET	1.96	0.84	5	5.91	0.040	0.37	0.37
S-TOP	3.35	0.81	3	6.20	0.043	0.47	0.48
S-BER	1.88	0.84	4	4.46	0.043	0.28	0.28
P-KRI	3.30	0.64	(0.5)[#]	2.64	0.108	0.49	1.08
S-KRI	1.75	0.76	2.5	3.00	0.058	0.23	0.23
P-ave.			3	4.6		0.35	0.36
S-ave.			3.3	4.8		0.33	0.34

[#] Very doubtful α estimate.

Table 6. Inversion 6: TPLP model, $\alpha = 2.5$ constrained; search over H parameter.

Data set	100ψ	w_{av}	H	G & CV 10^{-3} km^{-1}		L_{200}	L_{1000}
P-SPN	2.53	0.63	30	5.27	0.048	0.32	0.33
S-SPN	2.21	0.80	30	5.68	0.033	0.35	0.36
P-PET	2.60	0.79	50	2.80	0.063	0.40	0.44
S-PET	2.00	0.84	40	4.59	0.041	0.38	0.39
S-TOP	3.30	0.81	30	8.54	0.042	0.52	0.54
P-BER[$]	3.82	0.79	[40]	4.76	0.080	0.40	0.41
S-BER	1.90	0.85	40	3.50	0.043	0.29	0.30
P-KRI	3.18	0.63	(90)[#]	2.27	0.108	0.40	0.45
P-KRI[$]	3.89	0.67	[40]	4.37	0.105	0.36	0.37
S-KRI	1.74	0.76	30	3.76	0.057	0.23	0.24
P-ave.	2.77	0.68	56			0.37	0.41
S-ave.	2.23	0.81	34			0.35	0.36

[$] Both H and α constrained.
[#] Very doubtful H estimate.

separately. Some Tables contain averages over results of the stations studied. As some individual station estimates are unreliable these averages are calculated over acceptable estimates only (the unacceptable values are those in parentheses).

Inversion 1 was applied to all 10 data sets, both for cases of residual-dependent weighting skipped and applied. Let us discuss its results. The values of rms residual ψ change radically when weighting is applied, and its critical role is evident. Most contaminated are the *P*-wave data, as manifested (as compared to *S*) both in larger ψ for the 'no weighting' case and in a smaller average weight for the 'weighting' case. In the case of the *P*-SPN data set, more than one-third of the initial data is rejected, whereas typical figures are 15–25 per cent. A special case is the *P*-TOP data set, where weighting is evidently incapable of supressing large errors.

Looking at g_e estimates, one notes that they decrease several times when weighting is applied. Some estimated g_e values are negative even with weighting applied, indicating data sets of doubtful value. We qualified as such and thus rejected the *P*-TOP data set with very high ψ, negative g_{e1} and very high t_{m0}, and the *P*-BER set with high ψ, negative g_{e2} and high t_{m0}. However, we later analyse the *P*-BER data set for the sake of comparison, with severe constraints applied. The data sets for BER, TOP and KRI are, generally, less informative, and this will be seen in further inversions as well.

As becomes evident from a comparison of 'no weighting' and 'weighting' cases, the parameter estimates depend mostly on the choice of a particular set of weights. The error related to a poor choice of weights is of a specific kind and has no manifestation in the formal error bounds of LS. Because of this limited value of formal errors, we made no effort to calculate formal error ranges for non-linear searches. To judge the real accuracy of our estimates comparisons should be made among the results of various inversions, and of various stations and wave types.

Now consider the t_{m0} estimates. It can be seen that they are rather scattered: some of them are evidently too small, while others are larger than a significant part of the observed data (so that if one would use them for correction and subtract them from data, one would obtain negative, physically meaningless corrected t_m values). A similar scatter was found in various other trial inversions. Note also that the averaging of values of t_{m0} estimates for the 'weighted' inversion over all reasonable *P*-wave data sets (with *P*-TOP and *P*-BER excluded) gives the value of 0.22 s, a value that is close to our *a priori* estimate of 0.18 s. We may assume that, although the estimation of t_{m0} is a reasonable idea and even produces, on average over all data sets, a quite realistic figure, the scatter of individual estimates is too large to permit the use of t_{m0} as a free parameter; that is to estimate it in each inversion, for each data set. In other words, we consider the scatter of t_{m0} estimates among data sets as essentially random, representing inversion inaccuracy. This point of view is supported by the noticeable negative correlation between t_{m0} and g_{e1} estimates which is quite understandable if caused by random error (because these two least-squares estimates are negatively correlated), but has no evident reason if considered as meaningful. Hence, we decided to constrain the t_{m0} value in all further inversions and to set it to the *a priori* estimated value of 0.18 s. The results of the constrained-t_m variant of Inversion 1 do not show any interesting points and thus are not given.

Inversion 2 (Table 2)

One can see that the results for *S*-BER, *S*-KRI and specifically *P*-KRI are less accurate (formal errors are above 40 per cent); note that for *S*-BER and *P*-KRI, g_{e3} estimates are negative. Among five better results, one can see that g_{e1}, for $h = 0$–20 km, is fairly stable among stations and wave types, with a large outlier value for *P*-PET only. As for g_{e2}, for $h = 20$–80 km, the results show a somewhat larger scatter, and the value for *P*-PET is the smallest, and of low accuracy. We consider the results for *P*-PET doubtful in this case. There is a possibility that the choice of layer boundaries is specifically unfavourable for this particular station: in the next inversion with another set of boundaries, the results are quite regular. As for g_{e3} for the lower half-space, its estimates have a scatter of one order of magnitude, and have large and comparable absolute errors (the scatter of relative errors given in the Table is caused by the scatter of the estimates themselves; this is the rare case where absolute errors would be preferable). Thus, only an order-of-magnitude estimate for g_{e3} can be deduced.

Inversion 3 (Table 3)

The general result of Inversion 2 is, as expected, fast g_e decay with depth. To see this decay more clearly, we tried to resolve a three-layer structure. However, we managed to obtain a marginally meaningful result only for stations SPN and PET, and, even for them, only for the three upper layers. For KRI, only g_{e1} and g_{e2} have any meaning; both g_{e3} and g_{e4} are considered unreliable. The averages over stations for Inversion 3 show in most detail the vertical g_e structure within the 0–100 km depth layer. An approach with PCP is, however, incapable of obtaining meaningful estimates for larger depths, and to obtain information on larger depths we made TPLP inversions.

Inversion 4 (Table 4 and Fig. 7)

Three TPLP inversions were performed, with a grid search over α, H or both. The grid over H had a constant step of 10 km, and that over α consisted of the following set of values: {0.5, 1, 1.5, 2, 3, 4, 5}. In each least-squares solution, the single parameter G was sought for (thus its formal error is inevitably too optimistic).

The first important general property of TPLP inversions is their markedly and systematically decreased residual error ψ as compared to the PCP case, giving this model a considerable advantage in general. In Inversion 4, we set both parameters α and H free. From Table 4 one can see that, for the relatively more informative data sets of SPN and PET, estimates of α and H are limited to the ranges of 2–4 and 30–70, respectively. For the other four data sets, ranges are wider (1.5–5 and 20–90 km), but this hardly reflects the real scatter. This viewpoint is supported by the fact of clear probably artificial positive correlation between α and H estimates. For this reason, we consider meaningful only inversions for SPN and PET. The estimates of H and α are, or course, rather rough. Their real accuracy can be seen from the fact that both these parameters, ideally, must be near to one another for *P*-wave and *S*-wave data inversions of the same station, because they both reflect highly correlated scatterer structures produced by the same inhomogeneity. In the actual inversion, the difference between H estimates from *P* and *S* inversions for PET and, similarly, between α values for SPN, is about twofold. At any rate, α is bracketed between 2 and 4, and H is between 30 and 70 km. The average H and α values are listed in Table 4. The estimates of G from Inversion 4 correspond to different layer thicknesses and should not be compared.

Inversion 5 (Table 5)

In an attempt to obtain more stable estimates for four less informative data sets, in Inversions 5 and 6 we fixed either H or α. In Inversion 5, the value of $H = 40$ km is constrained. It is chosen to be near to the average H estimate found in Inversion 4 (a comparable figure is also obtained in Inversion 6 with a fixed value of α, as will be seen soon). Estimates of α for TOP, BER and KRI, with the exception of *P*-KRI, all agree with the previous analysis made for SPN and PET based on results of Inversion 4, and give an average α of about 3. Of all the TPLP inversions, only here, at constant H, do we obtain G estimates that are comparable among stations.

Inversion 6 (Table 6)

Here the value $\alpha = 2.5$ is fixed based on the results of Gusev (1995); it is not far from the estimate of $\alpha \approx 3$ from Inversions 4 and 5. The main results here are the H and L_e estimates, which are mostly stable and meaningful, with some doubts as regards the *P*-KRI data set. We also tried to obtain an estimate for the *P*-BER data set (rejected in most inversions), fixing both $H = 40$ km and $\alpha = 2.5$. The result seems reasonable, and it is added to Table 6. In the same manner, the second estimate for *P*-KRI was obtained as well.

Optical thickness estimates

In addition to g_e estimates for various depths, we consider it useful to represent the integral loss properties of the entire profile by a single figure. A measure of such a kind is the effective optical thickness L_e (eq. 13 of Paper I—may also be written as $2\pi f t^*$). Logically simplest is the vertical optical thickness calculated for a vertical ray. However, for any seismological application we are most interested in the effect on a real inclined ray. Therefore we calculated the 'nearly vertical effective optical thickness' L_h of the upper layers of the Earth, calculated along a ray that starts at a depth h at an angle of incidence of 45°. The relative errors of L_h are calculated from errors of G or g_{ei} on the basis of the usual error transfer formula that accurately accounts for errors in G or g_{ei} and for correlations between estimates of g_{ei}. However, errors of estimation of H and α are not accounted for; hence, for the TPLP case, most interesting here, errors of L_h are underestimated. As was explained above, formal error estimates may be too low in general because of a certain arbitrariness of weighting. We believe that the scatter between stations bears more reliable information on the real range of errors; this is true both in general and specifically for L_h. This idea is supported by the analysis of the simulated inversion examples of Paper I. The particular h value chosen for illustration for the PCP cases is 200 km, so we cite the estimates of L_{200} in that group. In the TPLP cases we calculated two L_e estimates, L_{200} and L_{1000}, which are both meaningful. Both L_e estimates have in this case the same formal relative error as G.

Analysis of results

Now we discuss the results of the inversions as a whole. The first important point is that the g_{ei} results of Tables 1–6 show no clear indications of significant differences between stations. Be such differences real or not, our estimates are of too low an accuracy to resolve them. Thus we will confine our analysis to the joint estimates (Table 7 and Fig. 8), averaged over all stations (three or four for *P* waves and five for *S* waves). Two versions of each g_{ei} value are listed, for the following reason. As explained in Paper I, the inversion procedure is constructed on the basis of the oversimplified Gaussian-ACF heterogeneity model; hence, modification is needed in order to arrive at geophysically meaningful estimates that take into account a more realistic, self-affine, heterogeneity spectrum. In Paper I, after some discussion, the constant correction coefficient, equal to 2.0 for g_e, was proposed for this purpose. Hence, we cite the g_e values twice: as calculated, and also multiplied by 2.0 (marked by C). The values of the mean free path, $l_e = 1/g_e$, are also given. The relative (rms) error column is based both on the interstation scatter and on individual station accuracy; it contains our rough but realistic estimates of relative accuracy of the final average effective turbidity and mean free path values.

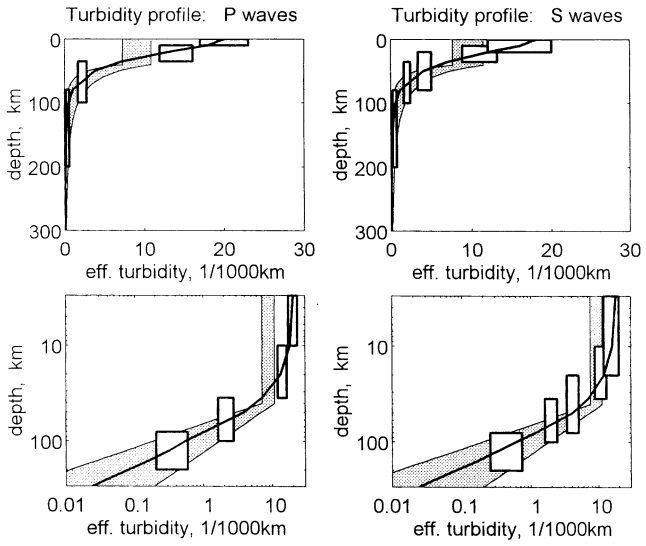

Figure 8. Estimated vertical profiles of average effective turbidity for *P* and *S* waves under Kamchatka, in common and log–log scales, based on summary values of Table 7. Boxes depict estimates from PCP inversions; their vertical size is $\pm 1\sigma$, and their horizontal size reflects the layer thickness assumed in a PCP inversion. The grey band shows the results of the TPLP inversion. For the horizonal (upper) part, the width of the band is based on $\pm 1\sigma$ for *G*; for the deeper part, the width reflects $\pm 1\sigma$ for *G* and the interval estimate for α ($\alpha = 2$–4) combined. The smooth line is the preliminary estimate of the profile function.

One can note a general consistency of estimates from different inversions. The initial idea of monotonic turbidity decay with depth is essentially confirmed. The only exclusions are the estimates for the 0–20 km and 0–10 km layers for *S* waves: here the 0–10 km layer estimate is insignificantly smaller. In general, the vertical effective turbidity profile cannot be compactly described either as a layer over a negligibly scattering half-space, or as a thin layer over a half-space with a power-law decay. Some structure is seen in the upper layers, with relatively slow general decay within the upper 40 km; the decay becomes fairly steep at larger depths, in general agreement with the power-law model. All attempts to introduce single upper layer within the PCP model resulted in a definitely worse fit than for the two- or three-layer models. However in terms of quality of fit, TPLP models are even better and the inverse power-law-like depth decay of effective turbidity below 40–60 km may be considered as well-founded. However, the numerical values of *G* obtained in TPLP Inversion 5 are somewhat lower than the expected value for the same 40 km layer that may be deduced from the layer estimates of Inversions 2 and 3. In our view, this slight systematic difference (note that it is larger for *P* waves where the accuracy for the 20–80 km layer is poor) may reflect a specific property of g_e estimates discussed in some detail in Part I. Namely, such estimates are not simply additive, so that the direct estimate for a thick layer need not coincide with the average over sublayers. In such a situation, we do not attach much importance to *G* estimates from Inversion 5.

Our data do not permit us to determine accurately the actual mode of depth decay, for the probable reason that our data sets have too small a proportion of (rare) events at depths greater than 160 km. The inverse power-law trend of Gusev (1995) had $\alpha = 2$–3. When this estimate is used as an *a priori* constraint by fixing $\alpha = 2.5$ in Inversion 6, the result did not show any features of a bad fit. However, attempts to estimate this exponent independently gave, in the unconstrained Inversion 4 for SPN and PET, and in the depth-constrained Inversion 5 for other stations, a rather wide range of $\alpha = 2$–4. Therefore, one can infer that the present t_m data set can constrain only weakly the depth decay of g_e and it can be parametrized as $\alpha = 2$–4. In addition to the regular g_e estimates

Table 7. Average effective turbidity estimates (10^{-3} km^{-1} units) for layers*.

depth range	model type	*P* waves				*S* waves				g_{eP}/g_{eS}
		g_e	g_{eC}	l_{eC}, km	RE%	g_e	g_{eC}	l_{eC}, km	RE%	
0-10	PCP	10	20	50	15	7	14	70	20	1.4
0-20	PCP	10	20	50	50	8	16	62	25	1.2
10-35	PCP	7	14	70	15	5.5	11	90	20	1.25
20-80	PCP	1.4	2.8	350	50	2.1	4.2	240	20	0.7
35-100	PCP	1.1	2.2	450	25	1.0	2.0	500	20	1.1
80-200	PCP	0.2	0.4	2500	50	0.27	0.5	2000	50+	0.85
0-40	TPLP	4.6	9	110	20	4.8	9.5	105	20	0.95

* RE is the relative error.

discussed above, we have drawn continuous $g_e(h)$ profiles in Fig. 7. They represent our general understanding of the smoothed effective turbidity structure only and should not be treated as formal estimates.

For most inversions we calculated the values of L_{200}, and, for TPLP inversions, those of L_{1000}. Better estimates, from Inversions 3, 4 and 6, are compiled in Table 8. One can see that the estimates agree well among modes of inversion. The interstation scatter is 40 per cent. We cannot decide at present whether this represents a real phenomenon, or is related to random errors. All figures are given for oblique rays; for strictly vertical rays they must be multiplied by about 0.75.

Estimates of g_e for *P* waves are comparable to those for *S* waves. The layer ratios of *P*- to *S*-wave turbidities are cited in Table 7; they show considerable scatter, doubtfully of geophysical meaning. A gross estimate for the whole profile probably makes more sense. We calculated it from the values of L_h in Table 8; the average ratio is $L_{hP}/L_{hS} = g_{eS}/g_{eP} = 1.1$ (or $Q_S/Q_P = 1.90$). Most estimates of L_h have a formal accuracy of about 15–20 per cent, and for their average the figure is even better (± 10 per cent); the estimate of their ratio L_P/L_S has comparable accuracy because L_P and L_S are positively correlated. Based on interstation scatter, one can obtain more reliable and more conservative estimates of accuracy, of about 25 per cent, both for average L_h and their ratio.

DISCUSSION

For tens of years, the technicians of the data processing group of Kamchatkan seismological service have discriminated by eye earthquake populations with depths above and below the 30–50 km boundary ('crustal' and 'mantle' events), judging by the degree of visual 'clarity' of body-wave groups as seen on the photo-record (at the same hypocentral distance, 'mantle' events make much clearer onsets and shorter pulses). When the calculated hypocentre depth is doubtful, a technician regularly uses this fact to deduce the correct interval for depth (Gusev 1979). Thus the position of the boundary of the upper layer, located by TPLP inversions approximately at $h = 40$–45 km, is not at all unexpected. It is somewhat larger than the formal Moho depth of 30–35 km. One should keep in mind that horizontal variations of crustal thickness are prominent in the Kamchatka region, and also that the Moho boundary as such is often not unequivocally identified. At any rate, the high-turbidity layer cannot be directly identified with the crust. It matches much better the depth interval containing most seismicity: shallow events in the Kurile-Kamchatka island arc occupy the same depth interval, and the fast decay in the depth distribution of hypocentres begins at 45–50 km, comparable to the above-mentioned estimate of 40–45 km for the lower boundary of the high-turbidity layer.

Table 8. The values of effective optical thickness L_e.

Data set	L_{200}				L_{1000}	
	I3	I4/I6	AV	AVC	I6	I6C
P-SPN	0.37	0.30	0.33	0.66	0.33	0.66
S-SPN	0.37	0.35	0.36	0.72	0.36	0.72
P-PET	0.45	0.37	0.40	0.80	0.44	0.88
S-PET	0.41	0.40	0.40	0.80	0.39	0.78
S-TOP	(0.64)	0.52	0.50	1.00	0.54	1.08
P-BER	—	0.40	0.40	0.80	0.41	0.82
S-BER	(0.39)	0.29	0.28	0.56	0.30	0.60
P-KRI	(0.05)	0.40	0.40	0.80	0.45	0.90
S-KRI	(−0.09)	0.23	0.23	0.46	0.24	0.48
P-ave.	0.41	0.37	0.38	0.76	0.41	0.82
S-ave.	0.39	0.36	0.35	0.70	0.37	0.74
P/*S* ratio	1.05	1.03	1.08	1.08	1.10	1.10

I3, I4 and I6: results of inversions nos 3, 4, and 6; AV: average over inversions; AVC: same, corrected.

Abubakirov & Gusev (1990) estimated the mean free path around stations SPN and PET from the direct-wave-to-coda amplitude ratios, and obtained, for the 1.5, 3 and 6 Hz frequency bands, *S*-wave l estimates in the range 100–150 km for a coda lapse time of 20 s. These estimates can be regarded as indicating the average l_e value over the surface of the half-sphere of about 35 km radius around the station. These values agree fairly reasonably with our estimates of $l_{eC} = 62$ km and 240 km above and below the 20 km assumed boundary. Abubakirov & Gusev (1990) also give estimates of coda Q, or Q_c, as Q_c (3 Hz) = 540 for coda lapse times of 50 s; this value should be ascribed to the surface of a half-sphere of 90 km radius. It agrees with scattering Q values of 310–1100 (around 3 Hz) that follow from our g_e estimates for the same 0–20 km and 20–80 km layers.

On the basis of the determined g_e values we can make indirect estimates of some other parameters of interest. First, we can extrapolate our results, valid for the neighbourhood of 3 Hz, to a frequency of 1 Hz. There is a relatively well-established frequency dependence of *S*-wave scattering Q; it usually behaves like f^β [or $g(f) \propto f^{1-\beta}$], with $\beta = 0.7$–0.9 for tectonic regions, and one can assume a similar trend for *P* waves. For Kamchatka around Shipunski station, the $g_e(f)$ trend between 1.5 and 6 Hz was estimated by Abubakirov & Gusev (1990) as weakly expressed. Hence we set $\beta = 0.9$ for the rough numerical estimates below. In particular, one can extrapolate the estimated L_{1000} or g_e values to 1 Hz. In terms of the standard teleseismic loss parameter $t^* \equiv L/2\pi f$, this gives us the contributions of scattering to *P*-wave t^* on the receiver side of a teleseismic ray as $\delta t^*_{\text{receiver}} \approx 0.12$ at 1 Hz. For the focal side of a teleseismic ray, the similar $\delta t^*_{\text{focal}}$ parameter may vary from a value of about zero for a deep event, to a value equal to $\delta t^*_{\text{receiver}}$ for event at 1–2 km depth. Thus, neglecting the scattering contribution to t^* below 1000 km depth, one can give the range for the total scattering contribution to t^*, or δt^*, as $\delta t^*(1\text{ Hz}) = 0.12$–$0.24$. For the assumed reference earthquake depth of 20 km, one can assume $\delta t^* \approx 0.20$. For *S* waves, estimates are similar.

In the same manner we can estimate *S*-wave scattering losses for local to regional distances. Based on Table 7, we set *S*-wave effective turbidity values for the 0–20 and 20–40 km layers as $g_{e\,020} = 0.016\text{ km}^{-1}$ and $g_{e\,2040} = 0.007\text{ km}^{-1}$; we also fix the characteristic depth of a shallow Kamchatka event as 35 km. For a given hypocentral/ray distance, let us estimate the ray-average effective turbidity value as the weighted sum of the two listed figures, with the weights proportional to the relative ray lengths within each layer. For ray distances of 30, 100 and 300 km, the weights are, approximately, {1, 0}, {0.3, 0.7} and {0.1, 0.9}, giving the ray-average effective turbidity values of 0.0160, 0.0097 and 0.0079 km^{-1}, respectively. At $c_S = 3.5\text{ km s}^{-1}$ this gives ray-average scattering Q_S, or $Q_{\text{sc},S}$ (3 Hz), of 335, 555 and 680, or, for 1 Hz, assuming again $\beta = 0.9$, we obtain

$Q_{sc,S}$ (1 Hz) = 125, 205 and 255, respectively. These values are what we expect on the basis of our t_m analysis for the scattering contribution to Q for local/regional events.

Fedotov (1972) constructed the amplitude decay curve for *S*-wave magnitude determination for the same types of instruments and data as used here. Based on the estimated distance-dependent g_e values, one can find the power n in the usual $A \propto r^{-n}$ relationship that describes the amplitude curve. To do this, we assume: (1) geometrical spreading is $1/r$; (2) the observed amplitude behaves as (spectral energy/pulse duration)$^{0.5}$; and (3) pulse duration is proportional to distance. We also assume that the contribution of intrinsic loss to the total loss is small. A simple calculation gives $n \approx 1.8$ for $r = 50$–150 km, and $n \approx 2.1$ for $r = 100$–300 km. The actual shape of the amplitude curve, after its argument conversion from '*S*–*P*' to the distance *r* scale, follows $n \approx 2.0$ in the distance range $r \approx 40$–300 km. This compares reasonably with our estimate, giving a certain credibility to our assumptions, and suggesting that the contribution of intrinsic loss to total attenuation at regional distances is secondary, in agreement with the earlier estimates of $Q_i = 1000$–2000 of Dainty (1981) and Gusev (1995). Summing up the comparison to regional data, we note that the known properties of direct *S* waves and coda in Kamchatka are in reasonable agreement with our effective turbidity estimates.

We have no available data for *P* waves to compare. However, there is a piece of teleseismic evidence that can be used as an additional check on our approach. McLaughlin & Anderson (1987) studied the differential delay of teleseismic *P*-wave energy from explosions, on many station and arrays. They calculated the differences $\delta T = \langle T(5\text{ Hz})\rangle - \langle T(1\text{ Hz})\rangle$ and found them to be about $+0.5$ s, with large scatter. We will show that this observation agrees with our approach, with an additional assumption of slow g_e increase with frequency. For the numerical calculation, we again set $g_e \propto f^{1-\beta}$ with $\beta = 0.9$. To estimate $\langle T(f)\rangle$ one can use Bocharov's formula for the case where the observer and the source are each located on the surfaces of two Gaussian-ACF thin scattering layers of turbidities g_{e1} and g_{e2} and thicknesses h_1 and h_2, and the layers are separated by a thick non-scattering layer of thickness $r - h_1 - h_2$ ($h_1 \ll r$, $h_2 \ll r$). Then eq. (12) of Paper I gives

$$\langle T\rangle = (1/2c)(g_{e1}h_1^2 + g_{e2}h_2^2). \qquad (9)$$

Tentatively applying our g_e estimates, valid for 3 Hz, to both source and receiver structures, and fixing $g_{e1}h_1 = g_{e2}h_2 = L_{200} = 0.8$, $h_1 = h_2 = 40$ km, and $c = 8$ km s^{-1}, we obtain $\langle T(3\text{ Hz})\rangle = 4$ s. When $g_e \propto f^{0.1}$, this gives $\langle T(5\text{ Hz})\rangle = 4.2$ s, $\langle T(1\text{ Hz})\rangle = 3.6$ s, and $\delta T = 0.6$ s. Therefore, the observed δT value agrees well with the estimates based on our approach.

The idea of a truncated power-law vertical profile of effective turbidity (TPLP) was initially proposed by Gusev (1995) on the basis of the study of completely different data, those of coda *Q*, which reflect back scattering, as opposed to forward scattering analysed here. On the whole, this idea agrees with the results of this study. However, as could be expected, the real structure is not as simple as the primitive TPLP. The values of the exponent α of the inverse power-law decay were bracketed as 1.5–3 in the previous paper. The range obtained here (2–4) bears no real contradiction, although no improvement of accuracy.

The ratio $\zeta = Q_S/Q_P$ estimated here as 1.9 can be compared to the theoretical estimate given by Sato (1990) for an inhomogeneity field with a von Karman autocorrelation function. For high frequencies (essentially, the self-affine case) he estimated $\zeta \approx 1.64 + 1.5\kappa$, where κ is the parameter of the von Karman function; this gives $\kappa \approx 0.17$, and the corresponding value of the exponent in the power-law inhomogeneity spectrum is equal to $\gamma = 3 + 2\kappa \approx 3.35$. This value can be compared to the preferred estimates of γ after Sato (1990) and Gusev & Abubakirov (1996b), both equivalent to $\gamma = 3.7$. These estimates are comparable; some difference may be expected because the analysis here is for an acoustic approximation and for effective turbidity, whereas Sato's estimates are for elastic waves and for 'true' turbidity.

CONCLUSIONS

We have performed a practical reconstruction of the vertical distribution of scattering properties of the Earth medium on the basis of the observed body-wave pulse broadening caused by forward scattering. In terms of effective turbidity, for the 2–5 Hz frequency range, the structure under Kamchatka can be described as a 40–50 km thick layer of gradually decreasing effective turbidity, underlain by a half-space with a fast decay of effective turbidity with depth; this decay approximately follows the inverse power law with an exponent of about three. This result is novel both methodically and in terms of a particular structure. An important point is that the upper layer does not coincide with the crust (30–35 km thick here); rather, the vertical effective turbidity profile resembles the vertical distribution of seismicity. The numerical values of effective turbidity estimates agree well with earlier turbidity estimates from coda waves, and the expected scattering loss grossly explains the shape of the standard Kamchatka amplitude attenuation (magnitude-calibration) curve. This suggests that the intrinsic loss is of secondary importance at relevant distances (50–300 km) and frequencies (2–4 Hz). Therefore, an important possibility occurs to deduce minimum attenuation estimates from pulse broadening data (or even, after proper calibration, to estimate intrinsic losses proper by subtracting scattering loss from total loss). An illustration developed here is the estimate of the lithospheric scattering contribution to the total teleseismic loss, of about $\Delta t_P^* = 0.20$ s at 1 Hz.

The technique developed here can be applied for the reconstruction of vertical effective turbidity profiles anywhere if observations can cover a considerably wide relative vertical range of hypocentral depths.

ACKNOWLEDGMENTS

The support of the Russian Foundation for Basic Research (project 93-05-08514) is gratefully acknowledged. We are indebted to the anonymous reviewer for valuable suggestions that improved the presentation.

REFERENCES

Abubakirov, I.R. & Gusev, A.A., 1990. Estimation of scattering properties of lithosphere of Kamchatka based on Monte-Carlo simulation of record envelope of a near earthquake, *Phys. Earth. planet Inter.*, **64,** 52–67.

Aki, K., 1973. Scattering of P-waves under Montana LASA, *J. geophys. Res.*, **78,** 1334–1346.

Aki, K., 1980. Scattering and attenuation of shear waves in the lithosphere, *J. geophys. Res.*, **85,** 6496–6504.

Aki, K. & Chouet, B., 1975. Origin of coda waves: source, attenuation and scattering effects, *J. geophys. Res.,* **80,** 3322–3342.

Bocharov, A.A., 1988. Mean delay and broadening of a pulse produced by scattering in the random inhomogeneous medium, *Izv. vuzov, Radiofizika,* **31,** 1407–1409 (in Russian).

Dainty, A.M., 1981. A scattering model to explain seismic *Q* observations in the lithosphere between 1 and 30 Hz, *Geophys. Res. Lett*., **8,** 1126–1128.

Fedotov, S.A., 1972. *Energy Classification of Kurile-Kamchatka Earthquakes and the Problem of Magnitudes,* Nauka, Moscow (in Russian).

Flatté, S.M. & Wu, R.-S., 1988. Small-scale structure in the lithosphere and asthenosphere deduced from arrival time and amplitude fluctuations at NORSAR, *J. geophys. Res.,* **93,** 6601–6614.

Gusev, A.A., 1979. Computer determination of hypocenters of near earthquakes in Kamchatka, *Vulkanol. Seism.,* No. 1, 74–81 (in Russian).

Gusev, A.A., 1995. Vertical profile of turbidity and coda *Q*, *Geophys. J. Int*., **123,** 665–672.

Gusev, A.A. & Abubakirov, I.R., 1996a. Study of the vertical turbidity profile of the lithosphere based on the inversion of body wave pulse broadening data, *Vulkanol. Seism.,* No. 4, 81–90 (see also English edition: 1997, **18,** 453–464).

Gusev, A.A., Abubakirov, I.R., 1996b. Simulated envelopes of non-isotropically scattered body waves as compared to observed ones: another manifestation of fractal inhomogeneity, *Geophys. J. Int.,* **127,** 49–60.

Gusev, A.A. & Abubakirov, I.R., 1999. Vertical profile of effective turbidity reconstructed from broadening of incoherent body wave pulses—I. General approach and the inversion procedure, *Geophys. J. Int.,* **136,** 295–308 (this issue).

Gusev, A.A. & Lemzikov, V.K., 1983. Estimation of scattering parameters of shear waves in the crust and upper mantle of Kamchatka according to observations of 'Shipunski' station, *Vulkanol. Seism.,* No. 1, 94–108.

Gusev, A.A. & Lemzikov, V.K., 1985. Properties of scattered elastic waves in the lithosphere of Kamchatka: parameters and temporal variations, *Tectonophysics,* **112,** 137–153.

Ishimaru, A., 1978. *Wave Propagation and Scattering in Random Media, vols 1 and 2,* Academic, San Diego, CA.

Jeffreys, H.K., 1961. *Theory of Probability,* Oxford University Press, Oxford.

McLaughlin, K.L. & Anderson, L.M., 1987. Stochastic dispersion ○ sort-period P-waves due to scattering and multipathing, *Geophys. J. R. astr. Soc.,* **89,** 933–963.

Rautian, T.G., Khalturin, V.I., Zakirov, M.S., Zemtsova, A.G., Proscurin, A.P., Pustovitenko, B.G., Pustovitenko, A.N., Sinelnikova, L.G., Filina, A.G. & Shengelia, I.S., 1981. *Experimental Studies of Seismic Coda,* Nauka, Moscow (in Russian).

Sato, H., 1989. Broadening of seismogram envelopes in the random inhomogeneous lithosphere based on the parabolic approximation: Southeastern Honshu, Japan, *J. geophys. Res.,* **94,** 17 735–17 747.

Sato, H., 1990. Unified approach to amplitude attenuation and coda excitation in the randomly inhomogeneous lithosphere, *Pure appl. Geophys.,* **132,** 93–119.

Williamson, I.P., 1972. Pulse broadening due to multiple scattering in the interstellar medium, *Mon. Not. R. astr. Soc.,* **157,** 55–71.

APPENDIX A: FORMULAE FOR THE COEFFICIENT a_{ij} IN (8) FOR A LAYER-OVER-HALF-SPACE VELOCITY PROFILE

We give an expression for the a_{1j} coefficient for the simple TPLP case, when both velocity and turbidity structures are (independently) of the kind 'a layer over a half-space'. h_j and h_M denote the depths of the source and of the velocity layer boundary (in practice the Moho); i_m and i_s, the incidence angles at the source and the station; $s_c = h_M/\cos i_s$, $v = H/(S \cos i_m)$, H, S, and α as above. Then, for $I = a_{1j}/S$, one obtains the following expressions by direct integration.

Case A: $H < h_M$.
Introduce $s_H = H/\cos i_s$, $u_H = s_H/S$, $u_c = s_c/S$,

$$w = h_j/(S \cos i_m) - 1\,, \qquad P = (w + u_c)/v\,, \qquad R = h_j/H\,.$$

See subcases A1, A21 and A22.

Case A1: $H < h_M$ and $h_j < H$: $I = 1/6$.

Case A21: $H < h_M$ and $h_j > H$ and $h_j < h_M$: $I = I_1 + I_2$, where

$$I_1 = u_H^2(1/2 - u_H/3);$$

$$I_2 = u_H^{\alpha}\{[1/(2-\alpha) - 1/(3-\alpha)] - [u_H^{2-\alpha}/(2-\alpha) - u_H^{3-\alpha}/(3-\alpha)]\}\,.$$

Case A22: $H < h_M$ and $h_j > H$ and $h_j > h_M$: $I = I_1 + I_2 + I_3$, where

I_1 as in Case A21:

$$I_2 = u_H^{\alpha}\{[u_c^{2-\alpha}/(2-\alpha) - u_c^{3-\alpha}/(3-\alpha)] - [u_H^{2-\alpha}/(2-\alpha) - u_H^{3-\alpha}/(3-\alpha)]\}\,;$$

$$I_3 = [v^3 P^{3-\alpha}/(3-\alpha) - v^2(2w+1)P^{2-\alpha}/(2-\alpha) + vw(1+w)P^{1-\alpha}/(1-\alpha)] - [v^3 R^{3-\alpha}/(3-\alpha) - v^2(2w+1)R^{2-\alpha}/(2-\alpha) + vw(1+w)R^{1-\alpha}/(1-\alpha)]\,.$$

Case B: $H > h_M$.
Introduce $s_H = s_c + (H - h_M/\cos i_m$, u_H as in A, $w = v - u_H$; $P = v$; $R = 1 + w$. See subcases B1 and B2.

Case B1: $h_j < H$, see A1.

Case B2: $h_j > H$, $I = I_1 + I_2$, where

$$I_1 = u_H^2(1/2 - u_H/3);$$

$$I_2 = v^{\alpha}\{[P^{3-\alpha}/(3-\alpha) - (2w+1)P^{2-\alpha}/(2-\alpha) + w(1+w)P^{1-\alpha}/(1-\alpha)]\} - \{[R^{3-\alpha}/(3-\alpha) - (2w+1)R^{2-\alpha}/(2-\alpha) + w(1+w)R^{1-\alpha}/(1-\alpha)]\}\,.$$